

Decomposition of the Reynolds shear stress in a turbulent boundary layer modified by miniature vortex generators

C. I. Chan * and R. C. Chin *School of Mechanical Engineering, University of Adelaide, South Australia 5005, Australia*

(Received 17 February 2022; accepted 27 April 2022; published 16 May 2022)

The investigation of the spanwise modulation of the Reynolds shear stress (RSS) distributions of a turbulent boundary layer modified by miniature vortex generators (MVGs) is performed, using an approach on a time-resolved velocity data set. The methodology is based on quadrant analysis of RSS to first identify the spatial and temporal information of the RSS events. We then apply the spanwise Fourier mode decomposition and triple velocity decomposition to obtain various statistics of the decomposed RSS events, including their conditional mean structures and actual mean skin friction contributions. In addition, the spanwise modification of the MVG on the RSS has been characterized by the fundamental and subharmonic modes of motions that scale with the spanwise separation distance (Λ_z) between MVG pairs. The interactions between the Λ_z^+ -scaled mode and subharmonic modes are further investigated using the scale-by-scale RSS transport equation [Kawata and Alfredsson, *Phys. Rev. Lett.* **120**, 244501 (2018)]. Results show that the Λ_z^+ -scaled motion tends to strengthen due to the inverse cascade of its subharmonic modes of motions, allowing the Λ_z^+ -scaled motion to persist further downstream.

DOI: [10.1103/PhysRevFluids.7.054603](https://doi.org/10.1103/PhysRevFluids.7.054603)

I. INTRODUCTION

A useful device for the study of passive control of flat plate boundary layers is the miniature vortex generator (MVG). For example, recent studies have illustrated the ability of MVG to generate streamwise orientated vortices that give rise to long and persistent streamwise streaks that evolve downstream in boundary layer flows. The MVG has gained interest owing to its simplicity and ease of manufacturing [1,2]. The characteristics of MVG in laminar boundary layers have been widely explored in both experimental and numerical studies. Single and consecutive arrays of MVGs mounted in a flat-plate boundary layer can delay flow transition from laminar to turbulent through Tollmien-Schlichting waves or oblique disturbance attenuations, results in a substantial skin friction reduction [1–5]. Experimental and numerical investigations of flow modifications by MVGs in turbulent wall-bounded flows were limited. Experimental studies were mainly conducted to investigate flow separation controls by vortex generators in adverse-pressure gradient and zero-pressure gradient turbulent boundary layers (ZPG TBLs) [6]. The flow dynamic related to streamwise evolution of the MVG-induced vortices persisting for up to $300h$ (where h is the device height) has been studied in subsequent work [7].

Flow that exhibits spatial heterogeneity perpendicular to the flow direction (e.g., spanwise periodicity) is often analyzed by the triple decomposition of velocity fluctuations, for example, for flows over canopy model [8–10], where the total velocity fluctuation can be decomposed into turbulent and coherent fluctuations. The turbulent fluctuation is associated with the velocity fluctuation about

*chiip.chan@adelaide.edu.au

the time-averaged velocity and the coherent fluctuation is a spatial fluctuation that arise from the turbulent fluctuation due to spatial heterogeneity. The coherent fluctuation arose due to spanwise periodicity introduced by MVG were treated in a similar fashion, as demonstrated by Shahinfar *et al.* [11] and recently studied by Chan and Chin [12] in TBL. In our previous work [12], we studied the flow modification of large-scale counter-rotating primary vortex pairs, such as low-speed streaks formation and streamwise turbulence intensity, and based on kinetic observations, the evaluation of the energy transfer among three components of the triple decomposed kinetic energy. However, the influence of MVG on the Reynolds shear stress (RSS) has not been examined in any detail. In this paper, we extend our previous work to investigate the RSS in terms of triple velocity decomposition and scale decomposition. From the viewpoint of studying of turbulent shear flows, the RSS can be viewed as an important quantity for their importance in the mean momentum transport and turbulent kinetic energy production, and their contributions in the large-scale and very-large-scale motions [13–15], as well as their weighted wall-normal distribution to the skin friction coefficient through the mean momentum transport equation [16,17]. The RSS can be quantified by an analysis of its signs [18], where an ejection event is related to the Q_2 motion, defined as $u'' < 0$ and $v'' > 0$, where u'' and v'' are the velocity fluctuations with respect to their global mean values Eq. (3) in the streamwise and wall-normal direction, and a sweep event is related to the Q_4 motion (where $u'' > 0$ and $v'' < 0$). The quadrant analysis of RSS provides a quantitative evaluation of the ejection and sweep events that observed in the work of Corino and Brodkey [19], which are related to the Q_2 and Q_4 motions and the major fractional contributions to the RSS [20–22]. The other two quadrants are the Q_1 and Q_3 motions defined as $u'' > 0$ and $v'' > 0$ and $u'' < 0$ and $v'' < 0$, and refer to the outward and inward interactions [18]. The quadrant analysis has gained interest in ejection and sweep-type events as fundamental elements of turbulent wall-bounded flows and has generated ideas for flow research based on the quadrant classification of the momentum, heat, and vorticity covariances.

In this paper, we study the flow modification of MVGs set up in a moderate Reynolds number ZPG TBL, motivated by the recent experimental studies of Lögberg *et al.* [7], Sattarzadeh *et al.* [5] and Sattarzadeh and Fransson [23]. The specific aims are to (i) employ the quadrant analysis of RSS adopted with spanwise scale decomposition to investigate the large- and small-scale components of the RSS and (ii) provide insights into their temporal and spatial properties under the influence of MVGs using triple velocity decomposition. The present paper aims to provide insight into the structural representation of the turbulent wall-bounded flow, which is of fundamental importance for turbulent flow research.

The remainder of this paper is organized as follows. In Sec. II, we present the numerical procedure and Sec. III the methodology of analysis. Results are presented in Sec. IV and conclusions are presented in Sec. V.

II. NUMERICAL PROCEDURE

In the following, the streamwise, wall-normal, and spanwise coordinates are denoted as $\mathbf{x} = (x, y, z)$ or x_i , and their velocity components are denoted as $\mathbf{u} = (u, v, w)$ or u_i , respectively. The present paper is based on the data set of Chan and Chin [12], hereafter referred to as MVG2021. The MVG is modeled by the introduction of an additional volume force field to the Navier-Stokes equations, based on the immersed boundary method [24], as discussed and validated in Chan and Chin [12]. The MVG configuration is shown in Figs. 1(a) and 1(b). The MVG array is positioned at $x_M = 950\delta_0^*$ from the inlet, corresponding to $\text{Re}_\tau = \delta^+ \simeq 430$, where δ_0^* is the inlet displacement thickness and δ is the boundary layer thickness. The superscript $+$ refers to scaling with the shear velocity $u_\tau = \sqrt{\tau_w/\rho}$ and kinematic viscosity ν , where τ_w is the wall shear stress and ρ is the fluid density. The MVG parameters that scale with the inlet displacement thickness are, respectively, $h = 4\delta_0^*$ is the device height, $t_m = 1\delta_0^*$ is the blade thickness (where $t_m \simeq 3.2$ grid points in the spanwise direction), $L_x = 10\delta_0^*$ is the blade length, $\alpha = 15^\circ$ is the angle of attack of the MVG with respect to the flow direction, $d_z = 10\delta_0^*$ is the spanwise distance between the centroids of blades in one

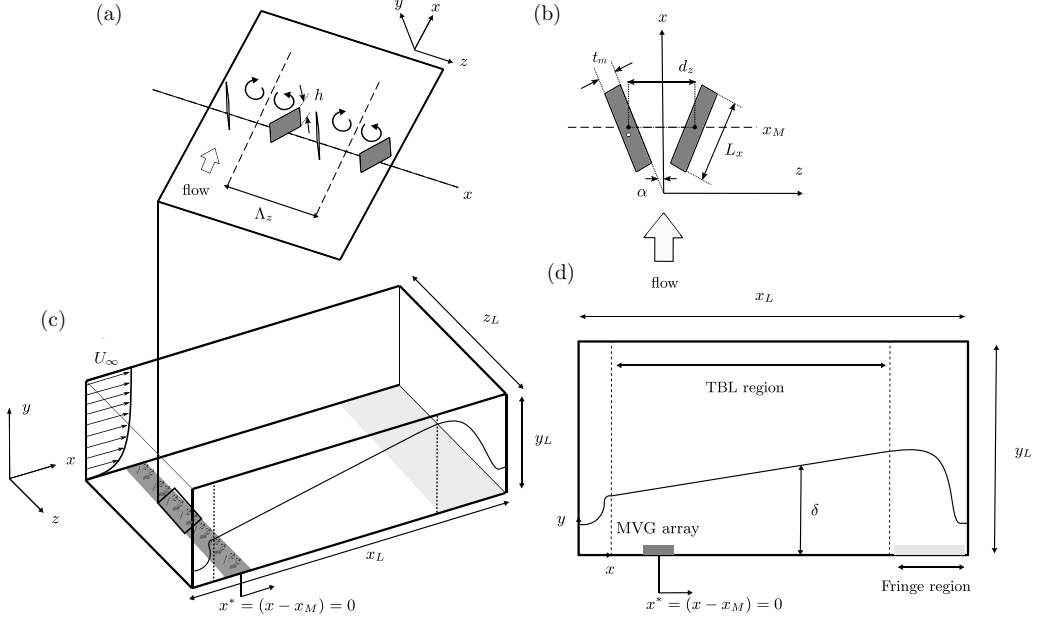


FIG. 1. (a), (b) Schematic of the MVG layouts considered in the present paper. The MVG parameters are scaled by the inlet displacement thickness δ_0^* . Here, $h = 4\delta_0^*$ is the device height, $t_m = 1\delta_0^*$ is the blade width, $L_x = 10\delta_0^*$ is the blade length, $\alpha = 15^\circ$ is the angle of attack of the MVG with respect to the flow direction, $d_z = 10\delta_0^*$ is the spanwise distance between the centroids of blades in one pair, and $\Lambda_z = 40\delta_0^*$ is the spanwise spacing between MVG pairs. (c), (d) Schematic of the TBL numerical domain with a MVG array. The domain size is $x_L \times y_L \times z_L = 6000\delta_0^* \times 200\delta_0^* \times 360\delta_0^*$, with a MVG array positioned at $x_M = 950\delta_0^*$, corresponding to $\text{Re}_\tau = \delta^+ \simeq 430$, where δ is the boundary layer thickness.

pair, and $\Lambda_z = 40\delta_0^*$ is the spanwise spacing between MVG pairs. The large-eddy simulation of a turbulent boundary layer was performed using a fully spectral numerical code [25]. A sub-grid-scale approximate deconvolution model (ADM-RT) has been employed to compute approximations to the unfiltered solutions of the incompressible continuity and Navier-Stokes equations by a repeated filter operation [26],

$$\frac{\partial \hat{u}_i}{\partial x_i} = 0, \quad (1)$$

$$\frac{\partial \hat{u}_i}{\partial t} + \hat{u}_j \frac{\partial \hat{u}_i}{\partial x_j} + \frac{\partial \hat{p}}{\partial x_i} - \frac{1}{\text{Re}} \frac{\partial^2 \hat{u}_i}{\partial x_j \partial x_j} = -\chi H_N \otimes \hat{u}_i, \quad (2)$$

where superscripts \wedge refer to a resolved-scale, \otimes denotes the convolution, the relaxation term $-\chi H_N \otimes \hat{u}_i$: χ is the model coefficient, and $H_N \otimes \hat{u}_i$ is the high-pass approximately deconvolved quantities. The ADM-RT model has been shown to be accurate and robust in predicting incompressible transitional and turbulent flows [26–29]. Spatial discretization is based on a Fourier series with 3/2 zero padding for de-aliasing in the streamwise (x) and spanwise (z) directions, and a Chebyshev polynomial is employed in the wall-normal direction (y). A schematic of the computational domain is shown in Figs. 1(c) and 1(d). The computational domain in the streamwise, wall-normal, and spanwise directions are, respectively, $x_L \times y_L \times z_L = 6000\delta_0^* \times 200\delta_0^* \times 360\delta_0^*$ using $6144 \times 513 \times 768$ spectral modes, with uniform grid spacings of $\Delta x^+ \approx 16.9$ and $\Delta z^+ \approx 8.1$ in the streamwise and spanwise directions. In the wall-normal direction, there are at least 15 Chebyshev collocation points within the region $y^+ < 10$. The first grid point away from the wall is at $y^+ \approx 0.03$, and the maximum spacing is $\Delta y_{\text{max}}^+ = 10.6$. A fringe region is employed at the end of the computational domain and

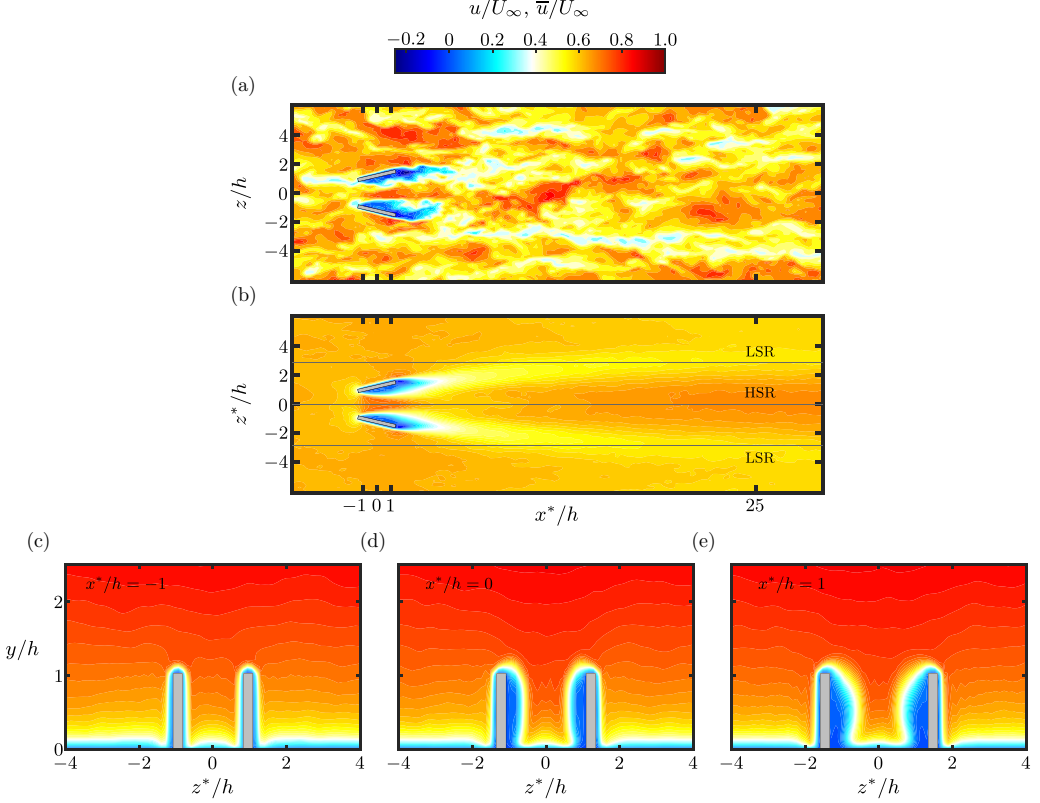


FIG. 2. (a) Instantaneous realization of the streamwise velocity flow field, u/U_∞ , at $y/h = 0.5$ around a pair of MVGs. Top view (b) and cross-section views of the time-averaged streamwise velocity flow field, \bar{u}/U_∞ , at (c) $x^*/h = -1$, (d) $x^*/h = 0$, and (e) $x^*/h = 1$, where $x^* = x - x_M$. Rectangular box outlines the MVG cross section. In (b), the solid black lines mark the spanwise locations of high-speed region (HSR) and low-speed region (LSR) at $x^*/h = 25$, respectively.

the flow is damped via a volume force to retain periodic boundary conditions in the streamwise direction. A low-amplitude volume force trip is applied to trigger the transition to turbulent flow at the inlet region [30]. The time advancement is carried out by a second-order Crank-Nicolson scheme for the viscous terms and a third-order four-stage Runge-Kutta scheme for the nonlinear terms. In this paper, time-averaged quantity is denoted by a $\bar{(\cdot)}$, and its fluctuation is denoted by a prime $(\cdot)'$ [see Eq. (3)]. The simulation has been performed for at least $\Delta T u_\tau^2/\nu \approx 8340$ (or ≈ 8.8 eddy turnover time at $\text{Re}_\tau \approx 1000$) before we started to gather data. The results shown in this paper (i.e., Figs. 3–8) are sampled for $\Delta T u_\tau^2/\nu \approx 7300$ (or ≈ 7.7 eddy turnover time). In addition, the mean-flow realizations (i.e., Fig. 2) presented in this paper used 86 full flow fields, each with sufficient time span so each field file is considered as statistically independent. The time-averaged quantity is further averaged over the periodic spanwise direction. The periodic spanwise coordinate is denoted as $z^* = \text{modulo}(z, \Lambda_z)$ within each MVG pair, i.e., $f(x, y, z^*) = 1/(N + 1) \sum_{n=0}^N f(x, y, z + n\Lambda_z)$. Figure 2 shows the instantaneous and time-averaged streamwise velocity fields obtained in the streamwise-spanwise plane at $y/h = 0.5$ [Figs. 2(a) and 2(b)], and spanwise-wall-normal plane at $x^*/h = -1$, 0, and 1 of the time-averaged streamwise velocity field [Figs. 2(c)–2(e)], where $x^* = x - x_M$ is defined at the center of a MVG. Spanwise alternating high- and low-speed patterns are observed with a high-speed region (HSR) formed along the center line of the MVG, accompanied with low-speed region (LSR) to the side-by-side region. The HSR and LSR have

been shown to be associated with skin friction variation up to $\pm 10 - 15\%$ at $x^*/h \simeq 25 - 50$ [12], respectively.

III. ANALYSIS OF THE REYNOLDS SHEAR STRESS FIELD

A. Velocity fluctuation decomposition

The presence of the MVG array introduces a strong spanwise modulation effect on the velocity fluctuations [1, 11, 12]. To investigate the spatial variations of velocity fluctuations due to such spanwise modulation, we adopted the approach to analyze roughness surface flow by triple decomposition of the velocity components, which reads as

$$u_i(\mathbf{x}, t) = \bar{u}_i(\mathbf{x}) + u'_i(\mathbf{x}, t) = \langle \bar{u}_i \rangle(x, y) + \underbrace{u'_i(\mathbf{x}, t) + \tilde{u}_i(\mathbf{x})}_{u''_i} \quad (3)$$

The symbol $\langle \cdot \rangle$ denotes a mean value over the span. u'_i and \tilde{u}_i on the right-hand side of Eq. (3) are the turbulent and coherent fluctuations, respectively. The coherent fluctuations \tilde{u}_i represent the induced-spatial variation of the time-averaged flow due to the presence of MVGs. The total fluctuations are $u''_i \simeq u'_i$ for the smooth wall case without MVGs since $\tilde{u}_i \simeq 0$.

B. Fourier mode decomposition of velocity fluctuations

We analyze the RSS fields based on a Fourier mode decomposition. After the instantaneous velocities, u_i are split into their global means $\langle \bar{u}_i \rangle(x, y)$ and their deviations $u'_i(\mathbf{x}, t)$, we apply a sharp spatial filtering based on a spanwise cutoff wave number $\lambda_{z,c} = 2\pi/k_{z,c}$ to the total velocity fluctuation fields $u''_i(\mathbf{x}, t)$. The scale decomposition can be expressed as

$$u''_i(\mathbf{x}, t) = u''_{i,L}(\mathbf{x}, t; k_{z,c}) + u''_{i,S}(\mathbf{x}, t; k_{z,c}), \quad (4)$$

where the total velocity fluctuations are expressed as superposition of the large-scale fluctuations ($u''_{i,L}$) and small-scale fluctuations ($u''_{i,S}$). Here, subscripts L and S denote the large-scale and small-scale components, respectively. Moreover, it can be shown that the scale decomposition is equivalent to

$$u''_{i,L}(\mathbf{x}, t; k_{z,c}) = u'_{i,L}(\mathbf{x}, t; k_{z,c}) + \tilde{u}_{i,L}(\mathbf{x}, t; k_{z,c}), \quad (5)$$

$$u''_{i,S}(\mathbf{x}, t; k_{z,c}) = u'_{i,S}(\mathbf{x}, t; k_{z,c}) + \tilde{u}_{i,S}(\mathbf{x}, t; k_{z,c}), \quad (6)$$

where (\prime) and $(\tilde{})$ denote the turbulent and coherent velocity fluctuations based on triple decomposition Eq. (3), respectively. Given that

$$u''_i u''_j(\mathbf{x}, t) = u''_{i,L} u''_{j,L}(\mathbf{x}, t; k_{z,c}) + u''_{i,L} u''_{j,S}(\mathbf{x}, t; k_{z,c}) + u''_{i,S} u''_{j,L}(\mathbf{x}, t; k_{z,c}) + u''_{i,S} u''_{j,S}(\mathbf{x}, t; k_{z,c}), \quad (7)$$

then the Reynolds stresses satisfy the scale decomposition as

$$\overline{u''_i u''_j}(\mathbf{x}) = \overline{u''_{i,L} u''_{j,L}}(\mathbf{x}; k_{z,c}) + \overline{u''_{i,S} u''_{j,S}}(\mathbf{x}; k_{z,c}), \quad (8)$$

and they also satisfy the triple decomposition as

$$\overline{u''_{i,L} u''_{j,L}}(\mathbf{x}; k_{z,c}) = \overline{u'_{i,L} u'_{j,L}}(\mathbf{x}; k_{z,c}) + \tilde{u}_{i,L} \tilde{u}_{j,L}(\mathbf{x}; k_{z,c}), \quad (9)$$

$$\overline{u''_{i,S} u''_{j,S}}(\mathbf{x}; k_{z,c}) = \overline{u'_{i,S} u'_{j,S}}(\mathbf{x}; k_{z,c}) + \tilde{u}_{i,S} \tilde{u}_{j,S}(\mathbf{x}; k_{z,c}). \quad (10)$$

Additionally, the one-dimensional spanwise wave-number cospectra of $-u'' v''$, $-u' v'$, and $-\tilde{u} \tilde{v}$ can be expressed as

$$-\overline{u''_L v''_L}(x, y; k_{z,c}) = \int_0^{k_{z,c}} \phi''_{-uv}(x, y, k_z) dk_z, \quad -\overline{u''_S v''_S}(x, y; k_{z,c}) = \int_{k_{z,c}}^{\infty} \phi''_{-uv}(x, y, k_z) dk_z, \quad (11)$$

$$-\langle \overline{u'_L v'_L} \rangle(x, y; k_{z,c}) = \int_0^{k_{z,c}} \phi'_{-uv}(x, y, k_z) dk_z, \quad -\langle \overline{u'_S v'_S} \rangle(x, y; k_{z,c}) = \int_{k_{z,c}}^{\infty} \phi'_{-uv}(x, y, k_z) dk_z, \quad (12)$$

$$-\langle \tilde{u}_L \tilde{v}_L \rangle(x, y; k_{z,c}) = \int_0^{k_{z,c}} \tilde{\phi}_{-uv}(x, y, k_z) dk_z, \quad -\langle \tilde{u}_S \tilde{v}_S \rangle(x, y; k_{z,c}) = \int_{k_{z,c}}^{\infty} \tilde{\phi}_{-uv}(x, y, k_z) dk_z, \quad (13)$$

for the large-scale and small-scale contributions, respectively.

C. Quadrant analysis of RSS

We further adopt the quadrant analysis of RSS [18]. The total RSS can be expressed as $u''v'' = \sum_{n=1}^4 Q''_n$, where Q''_n denotes the n th quadrant of (u'', v'') plane, e.g., $Q''_2 = \{u''v'' \mid u'' < 0, v'' > 0\}$. Utilizing quadrant analysis of RSS, the large-scale component of the total RSS events can be defined as

$$\begin{aligned} Q''_{1L}(\mathbf{x}, t; k_{z,c}) &= \{u''_L v''_L \mid u'' > 0, v'' > 0\}, & Q''_{2L}(\mathbf{x}, t; k_{z,c}) &= \{u''_L v''_L \mid u'' < 0, v'' > 0\}, \\ Q''_{3L}(\mathbf{x}, t; k_{z,c}) &= \{u''_L v''_L \mid u'' < 0, v'' < 0\}, & Q''_{4L}(\mathbf{x}, t; k_{z,c}) &= \{u''_L v''_L \mid u'' > 0, v'' < 0\}, \end{aligned} \quad (14)$$

where the small-scale component of total RSS events (Q''_S) and the large- and small-scale interactions (Q''_{LS}) and (Q''_{SL}) are obtained in a similar manner as Eqs. (14), and are given by

$$\begin{aligned} Q''_{1LS}(\mathbf{x}, t; k_{z,c}) &= \{u''_L v''_S \mid u'' > 0, v'' > 0\}, & Q''_{2LS}(\mathbf{x}, t; k_{z,c}) &= \{u''_L v''_S \mid u'' < 0, v'' > 0\}, \\ Q''_{3LS}(\mathbf{x}, t; k_{z,c}) &= \{u''_L v''_S \mid u'' < 0, v'' < 0\}, & Q''_{4LS}(\mathbf{x}, t; k_{z,c}) &= \{u''_L v''_S \mid u'' > 0, v'' < 0\}, \end{aligned} \quad (15)$$

$$\begin{aligned} Q''_{1SL}(\mathbf{x}, t; k_{z,c}) &= \{u''_S v''_L \mid u'' > 0, v'' > 0\}, & Q''_{2SL}(\mathbf{x}, t; k_{z,c}) &= \{u''_S v''_L \mid u'' < 0, v'' > 0\}, \\ Q''_{3SL}(\mathbf{x}, t; k_{z,c}) &= \{u''_S v''_L \mid u'' < 0, v'' < 0\}, & Q''_{4SL}(\mathbf{x}, t; k_{z,c}) &= \{u''_S v''_L \mid u'' > 0, v'' < 0\}, \end{aligned} \quad (16)$$

$$\begin{aligned} Q''_{1S}(\mathbf{x}, t; k_{z,c}) &= \{u''_S v''_S \mid u'' > 0, v'' > 0\}, & Q''_{2S}(\mathbf{x}, t; k_{z,c}) &= \{u''_S v''_S \mid u'' < 0, v'' > 0\}, \\ Q''_{3S}(\mathbf{x}, t; k_{z,c}) &= \{u''_S v''_S \mid u'' < 0, v'' < 0\}, & Q''_{4S}(\mathbf{x}, t; k_{z,c}) &= \{u''_S v''_S \mid u'' > 0, v'' < 0\}. \end{aligned} \quad (17)$$

Here, the superscript ($''$) denotes the total component of the corresponding quadrant events. In the subscript, an integer denotes the n th quadrant and capital letter characterises the total RSS events as: large-scale component (L), small-scale component (S) and large- and-small-scale interactions (LS and SL). In addition, the quadrant decomposition can be expressed as

$$u''_L v''_L = \sum_{n=1}^4 Q''_{nL}, \quad u''_L v''_S = \sum_{n=1}^4 Q''_{nLS}, \quad u''_S v''_L = \sum_{n=1}^4 Q''_{nSL}, \quad u''_S v''_S = \sum_{n=1}^4 Q''_{nS}, \quad (18)$$

for each of the four components in Eq. (7). It can be shown that each of the total RSS events (Q''_n) can also be expressed as four categories (L, S, LS, and SL)

$$Q''_n(\mathbf{x}, t) = Q''_{nL} + Q''_{nLS} + Q''_{nSL} + Q''_{nS}, \quad \text{where } u''v'' = \sum_{n=1}^4 Q''_n, \quad (19)$$

for each quadrant of the (u'', v'') plane: $n = 1, 2, 3$, and 4, where on the right-hand side are the terms in Eqs. (18). To further examine the turbulent and coherent components of the quadrant events as identified above, we apply the triple decomposition scheme to the velocity fluctuation components. The turbulent component of the quadrant events is computed by following Eqs. (3), (4), and (14). We define the large-scale turbulent RSS as

$$\begin{aligned} Q'_{1L}(\mathbf{x}, t; k_{z,c}) &= \{u'_L v'_L \mid u'' > 0, v'' > 0\}, & Q'_{2L}(\mathbf{x}, t; k_{z,c}) &= \{u'_L v'_L \mid u'' < 0, v'' > 0\}, \\ Q'_{3L}(\mathbf{x}, t; k_{z,c}) &= \{u'_L v'_L \mid u'' < 0, v'' < 0\}, & Q'_{4L}(\mathbf{x}, t; k_{z,c}) &= \{u'_L v'_L \mid u'' > 0, v'' < 0\}, \end{aligned} \quad (20)$$

where Q'_{LS} , Q'_{SL} , and Q'_S are calculated in a similar fashion as in Eqs. (15)–(17), and are given by

$$\begin{aligned} Q'_{1LS}(\mathbf{x}, t; k_{z,c}) &= \{u'_L v'_S \mid u'' > 0, v'' > 0\}, & Q'_{2LS}(\mathbf{x}, t; k_{z,c}) &= \{u'_L v'_S \mid u'' < 0, v'' > 0\}, \\ Q'_{3LS}(\mathbf{x}, t; k_{z,c}) &= \{u'_L v'_S \mid u'' < 0, v'' < 0\}, & Q'_{4LS}(\mathbf{x}, t; k_{z,c}) &= \{u'_L v'_S \mid u'' > 0, v'' < 0\}, \end{aligned} \quad (21)$$

$$\begin{aligned} Q'_{1SL}(\mathbf{x}, t; k_{z,c}) &= \{u'_S v'_L \mid u'' > 0, v'' > 0\}, & Q'_{2SL}(\mathbf{x}, t; k_{z,c}) &= \{u'_S v'_L \mid u'' < 0, v'' > 0\}, \\ Q'_{3SL}(\mathbf{x}, t; k_{z,c}) &= \{u'_S v'_L \mid u'' < 0, v'' < 0\}, & Q'_{4SL}(\mathbf{x}, t; k_{z,c}) &= \{u'_S v'_L \mid u'' > 0, v'' < 0\}, \end{aligned} \quad (22)$$

$$\begin{aligned} Q'_{1S}(\mathbf{x}, t; k_{z,c}) &= \{u'_S v'_S \mid u'' > 0, v'' > 0\}, & Q'_{2S}(\mathbf{x}, t; k_{z,c}) &= \{u'_S v'_S \mid u'' < 0, v'' > 0\}, \\ Q'_{3S}(\mathbf{x}, t; k_{z,c}) &= \{u'_S v'_S \mid u'' < 0, v'' < 0\}, & Q'_{4S}(\mathbf{x}, t; k_{z,c}) &= \{u'_S v'_S \mid u'' > 0, v'' < 0\}, \end{aligned} \quad (23)$$

where the quadrant decomposition can be written as

$$u'_L v'_L = \sum_{n=1}^4 Q'_{nL}, \quad u'_L v'_S = \sum_{n=1}^4 Q'_{nLS}, \quad u'_S v'_L = \sum_{n=1}^4 Q'_{nSL}, \quad u'_S v'_S = \sum_{n=1}^4 Q'_{nS}. \quad (24)$$

Here, we make use of the (u'', v'') plane for the quadrant analysis so that the criterion is consistent to that we used in Eqs. (14)–(17), and thereby we are extracting the turbulent component of the quadrant events at the same (u'', v'') plane that we used in Eqs. (14)–(17). The (u'', v'') plane contains the temporal and spatial information of the quadrant events that we are interested in. It can be shown that using this criterion, we obtain

$$Q'_n(\mathbf{x}, t) = Q'_{nL} + Q'_{nLS} + Q'_{nSL} + Q'_{nS}, \quad \text{where} \quad u'v' = \sum_{n=1}^4 Q'_n, \quad (25)$$

for each quadrant of the (u'', v'') plane: $n = 1, 2, 3$, and 4. Finally, the coherent part of the quadrant events can be computed using the above methods because, following Eqs. (3)–(6), we can write

$$\begin{aligned} \underbrace{u''_{i,L} u''_{j,L}}_{(I)}(\mathbf{x}, t; k_{z,c}) &= \underbrace{u'_{i,L} u'_{j,L}}_{(II)} + \underbrace{u'_{i,L} \tilde{u}_{j,L}}_{(IVa)} + \underbrace{\tilde{u}_{i,L} u'_{j,L}}_{(IVa)} + \underbrace{\tilde{u}_{i,L} \tilde{u}_{j,L}}_{(III)}, \\ \underbrace{u''_{i,L} u''_{j,S}}_{(IVa)}(\mathbf{x}, t; k_{z,c}) &= \underbrace{u'_{i,L} u'_{j,S}}_{(IVa)} + \underbrace{u'_{i,L} \tilde{u}_{j,S}}_{(IVb)} + \underbrace{\tilde{u}_{i,L} u'_{j,S}}_{(IVb)} + \underbrace{\tilde{u}_{i,L} \tilde{u}_{j,S}}_{(IVa)}, \\ \underbrace{u''_{i,S} u''_{j,L}}_{(IVa)}(\mathbf{x}, t; k_{z,c}) &= \underbrace{u'_{i,S} u'_{j,L}}_{(IVa)} + \underbrace{u'_{i,S} \tilde{u}_{j,L}}_{(IVb)} + \underbrace{\tilde{u}_{i,S} u'_{j,L}}_{(IVb)} + \underbrace{\tilde{u}_{i,S} \tilde{u}_{j,L}}_{(IVa)}, \\ \underbrace{u''_{i,S} u''_{j,S}}_{(I)}(\mathbf{x}, t; k_{z,c}) &= \underbrace{u'_{i,S} u'_{j,S}}_{(II)} + \underbrace{u'_{i,S} \tilde{u}_{j,S}}_{(IVa)} + \underbrace{\tilde{u}_{i,S} u'_{j,S}}_{(IVa)} + \underbrace{\tilde{u}_{i,S} \tilde{u}_{j,S}}_{(III)}. \end{aligned} \quad (26)$$

Here, (I) are the large- and small-scale contributions of the total Reynolds stresses, (II) is the large- and small-scale contributions of the turbulent Reynolds stresses, (III) is the large- and small-scale contributions of the time-independent coherent Reynolds stresses, and (IV) is the time-dependent, zero-mean interactions: (IVa) denotes interactions either between large- and small-scale components or between turbulent and coherent components and (IVb) denotes cross-interactions between large- and small-scale components and turbulent and coherent components. Then we obtain the time-independent coherent part of the quadrant events using the relation Eqs. (26) by assigning $i = 1$ and $j = 2$ and then taking the time average, and we extract the coherent part of the quadrant events on the same (u'', v'') plane that we defined previously for the total and turbulent component of the quadrant events:

$$\begin{aligned} \tilde{Q}_{nL}(\mathbf{x}; k_{z,c}) &= \overline{Q''_{nL}} - \overline{Q'_{nL}}, & \tilde{Q}_{nLS}(\mathbf{x}; k_{z,c}) &= \overline{Q''_{nLS}} - \overline{Q'_{nLS}}, \\ \tilde{Q}_{nSL}(\mathbf{x}; k_{z,c}) &= \overline{Q''_{nSL}} - \overline{Q'_{nSL}}, & \tilde{Q}_{nS}(\mathbf{x}; k_{z,c}) &= \overline{Q''_{nS}} - \overline{Q'_{nS}}. \end{aligned} \quad (27)$$

More importantly, because of Eqs. (18), (24), and (26), the coherent components of the RSS satisfy

$$\begin{aligned} \sum_{n=1}^4 \tilde{Q}_{nL} &= \sum_{n=1}^4 \overline{Q''}_{nL} - \sum_{n=1}^4 \overline{Q}'_{nL} = \tilde{u}_L \tilde{v}_L, & \sum_{n=1}^4 \tilde{Q}_{nLS} &= \sum_{n=1}^4 \overline{Q''}_{nLS} - \sum_{n=1}^4 \overline{Q}'_{nLS} = \tilde{u}_L \tilde{v}_S, \\ \sum_{n=1}^4 \tilde{Q}_{nSL} &= \sum_{n=1}^4 \overline{Q''}_{nSL} - \sum_{n=1}^4 \overline{Q}'_{nSL} = \tilde{u}_S \tilde{v}_L, & \sum_{n=1}^4 \tilde{Q}_{nS} &= \sum_{n=1}^4 \overline{Q''}_{nS} - \sum_{n=1}^4 \overline{Q}'_{nS} = \tilde{u}_S \tilde{v}_S, \end{aligned} \quad (28)$$

and it can be shown that

$$\tilde{Q}_n(\mathbf{x}) = \tilde{Q}_{nL} + \tilde{Q}_{nS} + \tilde{Q}_{nLS} + \tilde{Q}_{nSL} = \overline{Q''}_n - \overline{Q}'_n, \quad (29)$$

for each quadrant of coherent RSS: $n = 1, 2, 3,$ and 4 . Equations (18) illustrate that the four different components from specified $\lambda_{z,c}$ ranges [i.e., $\lambda_z > \lambda_{z,c}$ and $\lambda_z < \lambda_{z,c}$ in Eq. (7)] are directly associated with four quadrants of the (u'', v'') plane. Equations (19) show that if we sum the four different $\lambda_{z,c}$ -range components, we can reconstruct the same Q''_n that are obtained from the quadrants of the (u'', v'') plane. Therefore, Eqs. (19) imply that each Q''_n can be split into four groups: the large scales (L), the small scales (S), and the large- and small-scale interactions (LS and SL). Another feature of this decomposition is that it explicitly accounts for the effects of turbulent and coherent fluctuations [triple decomposition Eq. (3)] that often emerge in MVG or some rough-wall flows, as demonstrated in Eqs. (24), (25), (28), and (29). In the next section, we demonstrate that this decomposition can be used to split the mean skin friction generation due to RSS into different components and assess their relative contributions to the total mean skin friction coefficient. In particular, we also highlight the significance of the Q_2 and Q_4 events to the mean wall shear stress compared to the Q_1 and Q_3 events (as demonstrated in Secs. IV A and IV B).

D. Turbulent skin friction decomposition for MVG flows

This decomposition enables us to quantify the skin friction generation by different RSS events through the Fukagata-Iwamoto-Kasagi (FIK) identity [16]. The FIK identity is a momentum-based decomposition of the total mean skin friction coefficient C_f in TBL, which is given by a triple integration of the mean streamwise momentum equation over the wall [16]. The decomposition can be written as

$$C_f(x) = 2\tau_w/(\rho U_\infty^2) = C_{f,D} + C_{f,R} + C_{f,M} + C_{f,S}, \quad (30)$$

where τ_w , ρ , and U_∞ are the mean shear stress at the wall, incompressible fluid density, and free-stream velocity, respectively. $C_{f,D}$ denotes the contribution due to the laminar effect, $C_{f,R}$ denotes the contribution due to RSS (turbulent effect), $C_{f,M}$ and $C_{f,S}$ are related to the mean flow convection and spatial development of the TBL, respectively. More importantly, the mean skin friction generation by RSS, denoted as $C_{f,R}$, is given by

$$C_{f,R}(x) = \int_0^1 \underbrace{\left\langle \frac{4(1-y/\delta)}{U_\infty^2} [-\overline{u''v''}] \right\rangle}_{F''_R} d(y/\delta), \quad (31)$$

where F''_R is the weighed RSS contribution to the skin friction coefficient. From quadrant decomposition of the total RSS (Sec. III C), we first express the skin friction contribution by each quadrant as

$$-\overline{u''v''}(\mathbf{x}, t) = -\sum_{n=1}^4 Q''_n(\mathbf{x}, t), \quad F''_R(\mathbf{x}) = \frac{-4(1-y/\delta)}{U_\infty^2} \left[\sum_{n=1}^4 \overline{Q''}_n(\mathbf{x}) \right] = \sum_{n=1}^4 f''_{R,n}(\mathbf{x}), \quad (32)$$

where $f''_{R,n}(\mathbf{x}) = -4(1 - y/\delta) \bar{Q}''_n(\mathbf{x})/U_\infty^2$. The mean skin friction $C_{f,R}$ generated by each quadrant of RSS ($n = 1, 2, 3,$ and 4) can be obtained by integrating $\langle f''_{R,n} \rangle$ over the wall

$$C''_{R,n}(x) = \int_0^1 \langle f''_{R,n} \rangle d(y/\delta), \quad \text{where} \quad C_{f,R}(x) = \sum_{n=1}^4 C''_{R,n}. \quad (33)$$

Similarly, we have shown from Eqs. (8) and (18) that we can write F''_R as

$$\begin{aligned} \underbrace{F''_R(\mathbf{x})}_{\text{total}} &= \underbrace{\frac{-4(1-y/\delta)}{U_\infty^2} \left[\sum_{n=1}^4 \bar{Q}''_{nL}(\mathbf{x}; k_{z,c}) \right]}_{F''_{R,L, \text{ total}} \text{ large scale}} + \underbrace{\frac{-4(1-y/\delta)}{U_\infty^2} \left[\sum_{n=1}^4 \bar{Q}''_{nS}(\mathbf{x}; k_{z,c}) \right]}_{F''_{R,S, \text{ total}} \text{ small scale}} \\ &= \sum_{n=1}^4 \underbrace{[f''_{R,nL}]}_{\substack{\text{nth quadrant} \\ \text{total} \\ \text{large scale}}} + \sum_{n=1}^4 \underbrace{[f''_{R,nS}]}_{\substack{\text{nth quadrant} \\ \text{total} \\ \text{small scale}}}, \end{aligned} \quad (34)$$

where $f''_{R,nL} = -4(1 - y/\delta) \bar{Q}''_{nL}/U_\infty^2$ and $f''_{R,nS} = -4(1 - y/\delta) \bar{Q}''_{nS}/U_\infty^2$. Equation (34) demonstrates that the total F''_R can be split into eight components due to (i) n th quadrant events and (ii) large-scale or small-scale contributions. Furthermore, following Eqs. (9), (10), and (28), we can write $F''_{R,L}$ and $F''_{R,S}$ in Eq. (34) as

$$\begin{aligned} \underbrace{F''_{R,L}(\mathbf{x}; k_{z,c})}_{\text{total large scale}} &= \underbrace{\frac{-4(1-y/\delta)}{U_\infty^2} \left[\sum_{n=1}^4 \bar{Q}'_{nL}(\mathbf{x}; k_{z,c}) \right]}_{F'_{R,L, \text{ turbulent}} \text{ large scale}} + \underbrace{\frac{-4(1-y/\delta)}{U_\infty^2} \left[\sum_{n=1}^4 \tilde{Q}_{nL}(\mathbf{x}; k_{z,c}) \right]}_{\tilde{F}_{R,L, \text{ coherent}} \text{ large scale}} \\ &= \sum_{n=1}^4 \underbrace{[f'_{R,nL}]}_{\substack{\text{nth quadrant} \\ \text{turbulent} \\ \text{large scale}}} + \sum_{n=1}^4 \underbrace{[\tilde{f}_{R,nL}]}_{\substack{\text{nth quadrant} \\ \text{coherent} \\ \text{large scale}}}, \end{aligned} \quad (35)$$

$$\begin{aligned} \underbrace{F''_{R,S}(\mathbf{x}; k_{z,c})}_{\text{total small scale}} &= \underbrace{\frac{-4(1-y/\delta)}{U_\infty^2} \left[\sum_{n=1}^4 \bar{Q}'_{nS}(\mathbf{x}; k_{z,c}) \right]}_{F'_{R,S, \text{ turbulent}} \text{ small scale}} + \underbrace{\frac{-4(1-y/\delta)}{U_\infty^2} \left[\sum_{n=1}^4 \tilde{Q}_{nS}(\mathbf{x}; k_{z,c}) \right]}_{\tilde{F}_{R,S, \text{ coherent}} \text{ small scale}} \\ &= \sum_{n=1}^4 \underbrace{[f'_{R,nS}]}_{\substack{\text{nth quadrant} \\ \text{turbulent} \\ \text{small scale}}} + \sum_{n=1}^4 \underbrace{[\tilde{f}_{R,nS}]}_{\substack{\text{nth quadrant} \\ \text{coherent} \\ \text{small scale}}}, \end{aligned} \quad (36)$$

where, e.g., $f'_{R,nL} = -4(1 - y/\delta) \bar{Q}'_{nL}/U_\infty^2$. Finally, the mean skin friction generation by RSS, $C_{f,R}$, can be expressed as additive terms, accounting for: (i) n th quadrant events, (ii) large-scale and small-scale contributions, and (iii) turbulent and coherent stresses based on Eqs. (35) and (36), which lead to the following decomposition:

$$C_{f,R}(x) = \sum_{n=1}^4 C''_{R,nL} + \sum_{n=1}^4 C''_{R,nS} = \underbrace{\sum_{n=1}^4 C'_{R,nL}}_{\text{turbulent large scale}} + \underbrace{\sum_{n=1}^4 \tilde{C}_{R,nL}}_{\text{coherent large scale}} + \underbrace{\sum_{n=1}^4 C'_{R,nS}}_{\text{turbulent small scale}} + \underbrace{\sum_{n=1}^4 \tilde{C}_{R,nS}}_{\text{coherent small scale}}, \quad (37)$$

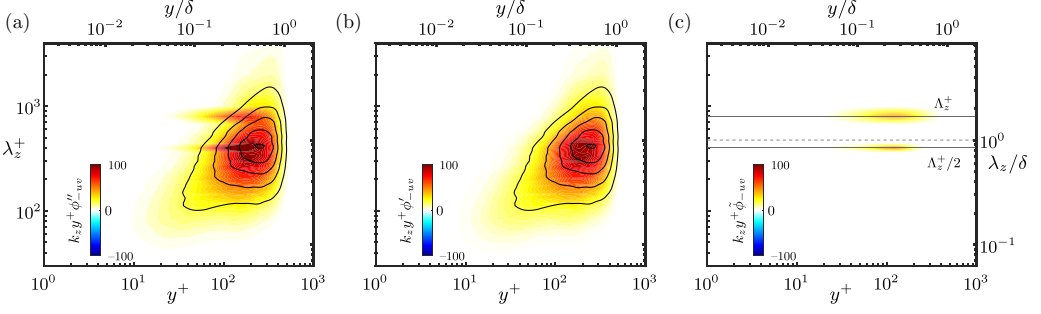


FIG. 3. The one-dimensional spanwise wave number premultiplied ($k_z y^+$) cospectra (colour contours) at $x^*/h = 25$ ($\text{Re}_\tau \simeq 470$). (a) Total RSS ($-u''v''$), $k_z y^+ \phi''_{-uv}$, (b) turbulent RSS ($-u'v'$), $k_z y^+ \phi'_{-uv}$, and (c) coherent RSS ($-\tilde{u}\tilde{v}$), $k_z y^+ \tilde{\phi}_{-uv}$. Black isolines: 20[20]100 in (a), (b) represent an unmanipulated DNS TBL (denoted as UBL in Sec. IV B) at $\text{Re}_\tau \simeq 500$ [31]. Black dashed line in (c) corresponds to the cutoff wavelength $\lambda_{z,c} = \delta$ used in the present paper, and two black solid lines denote the two observed energetic modes at Λ_z^+ and $\Lambda_z^+/2$.

where the mean skin friction generations for individual quadrant events can be obtained by integrations over the wall:

$$C''_{R,nL}(x; k_{z,c}) = \int_0^1 \langle f''_{R,nL} \rangle d(y/\delta), \quad C''_{R,nS}(x; k_{z,c}) = \int_0^1 \langle f''_{R,nS} \rangle d(y/\delta), \quad (38)$$

$$C'_{R,nL}(x; k_{z,c}) = \int_0^1 \langle f'_{R,nL} \rangle d(y/\delta), \quad C'_{R,nS}(x; k_{z,c}) = \int_0^1 \langle f'_{R,nS} \rangle d(y/\delta), \quad (39)$$

$$\tilde{C}_{R,nL}(x; k_{z,c}) = \int_0^1 \langle \tilde{f}_{R,nL} \rangle d(y/\delta), \quad \tilde{C}_{R,nS}(x; k_{z,c}) = \int_0^1 \langle \tilde{f}_{R,nS} \rangle d(y/\delta). \quad (40)$$

This decomposition [Eq. (37)] is consistent to the Eq. (33) [i.e., for each Q''_n of the (u'' , v'') plane], since the conditions Eqs. (19) and (25) hold for each quadrant ($n = 1, 2, 3$, and 4), so

$$\begin{aligned} C''_{R,n} &= C''_{R,nL} + C''_{R,nS} + C''_{R,nLS} + C''_{R,nSL} \\ &= \underbrace{C'_{R,nL} + C'_{R,nS} + C'_{R,nLS} + C'_{R,nSL}}_{\substack{\text{turbulent} \\ (\text{L, S, LS, SL})}} + \underbrace{\tilde{C}_{R,nL} + \tilde{C}_{R,nS} + \tilde{C}_{R,nLS} + \tilde{C}_{R,nSL}}_{\substack{\text{coherent} \\ (\text{L, S, LS, SL})}}, \end{aligned} \quad (41)$$

for $n = 1, 2, 3$, and 4. In the following, we will apply this approach to the data set obtained by the well-resolved large-eddy simulation to quantify the spanwise modification of RSS by the MVG. For the sake of brevity, some numerical results presented in the following of the paper are limited to the second and fourth quadrants (i.e., denoted by Q_2 and Q_4 , respectively), and their large- and small-scale components (i.e., denoted by subscripts L and S, respectively).

E. Choice of cutoff wave number

The choice of spanwise cutoff wave number can be quite arbitrary and depends on the research aims. We select the appropriate cutoff wave number based on the spanwise wave number premultiplied cospectra of $-u''v''$, $-u'v'$, and $-\tilde{u}\tilde{v}$. The spanwise wave number uv spectra has been adopted for the investigation of skin friction generation of turbulent channel flows (e.g., de Giovanetti *et al.* [17]). The MVG spanwise modulation is associated with the formation of high- and low-speed streaks behind the MVG pair, which is commonly reflected on the streamwise velocity spectra as a discrete set of peaks that scale with Λ_z^+ [12], where Λ_z is the spanwise spacing between two MVG pairs (see Fig. 1). Figure 3 presents the spanwise wave-number spectra ϕ''_{-uv} , ϕ'_{-uv} , and

$\tilde{\phi}_{-uv}$ at $x^*/h \simeq 25$ downstream of the MVG by introducing the triple decomposition of velocity fluctuations based on Eq. (3). As expected, two notable peaks were found [marked with solid lines in Fig. 3(c)], which correspond to the first two energetic modes that scale with Λ_z^+ , i.e., $\lambda_z^+ = \Lambda_z^+$ and $\lambda_z^+ = \Lambda_z^+/2$. Thus, we will consider a spanwise cutoff wavelength $\lambda_z \simeq \delta$. This corresponds to the wavelength marked with a dashed line in Fig. 3(c). Our attempt here is to assess the MVG-induced modification of the RSS as a superposition of the motions by (i) fundamental mode (i.e., Λ_z^+) and (ii) the subharmonic modes (i.e., $\Lambda_z^+/2$, $\Lambda_z^+/3$, and so forth). In the following, we let Λ_{z1}^+ denote the fundamental mode that scaled with Λ_z^+ and let Λ_{z2}^+ denote all the subharmonic modes (i.e., $\Lambda_z^+/2$, $\Lambda_z^+/3$, and so forth). Moreover, by utilizing this cutoff wavelength, we refer to the large scales as those with spanwise length scale $\lambda_z > \delta$ and the small scales as those with spanwise length scale $\lambda_z < \delta$.

IV. RESULTS AND DISCUSSION

A. Conditional fields of the total RSS and coherent RSS

We present the conditional large-scale field of the total RSS Q''_{2L} and Q''_{4L} at $x^*/h = 25$ in Fig. 4(a). Large-scale Q''_{4L} positions at the center ($z^* = 0$) and characterizes the HSR, adjacent with the side-by-side Q''_{2L} that is peaked at slightly higher y toward the outer region than that of Q''_{4L} ($Q''_{2L}^+ \simeq -0.125$ at $y \simeq 4h \simeq 0.68\delta$). On the other hand, the small-scale conditional field of total RSS Q''_{4S} and Q''_{2S} mainly resides toward the inner region, as shown in Fig. 4(b). We can observe that Q''_{4S} is centered at the HSR and Q''_{2S} is centered at the LSR in the inner region.

The large- and small-scale fields of the coherent RSS due to the secondary motions introduced by the MVG are plotted in Figs. 4(c)–4(f). \tilde{Q}_{2L} has a spanwise spacing reflecting the characteristic wavelength of the Λ_z^+ (i.e., the fundamental mode) that has been shown previously [Fig. 3(c)]. The slightly positive peak is centered at the HSR with two negative peaks that center along the side. Figures 4(c) and 4(e) suggest that the modulation effect of the MVGs can extend to a height of $5h$, therefore modifying the upper part of the TBL. \tilde{Q}_{4L} has a similar and consistent pattern but in the reverse order. It is noted that the negative peak is at a slightly lower wall-normal position than that of \tilde{Q}_{2L} , while the weak positive peak is at a higher wall-normal location compared to the positive peak in \tilde{Q}_{2L} . It is also noted that the positive \tilde{Q}_{2L} and \tilde{Q}_{4L} are almost fourfold lower than the negative counterparts, and they are roughly symmetrical with respect to the spanwise direction. Compared to the large-scale component, the modulation effects due to the small-scale component, i.e., the positive and negative \tilde{Q}_{2S} and \tilde{Q}_{4S} , are of similar magnitude, with a fairly uniform spanwise spacing predominantly reflecting the characteristic wavelength of mode $\Lambda_z^+/2$ [Figs. 4(d) and 4(f)]. These structures are confined to the lower part of the TBL and rarely observed in the outer region. A simplified schematic illustration of the correlations between total and coherent RSS events is proposed in Fig. 5 based on the observations in Fig. 4. The figure suggests that Q''_{2L} and Q''_{2S} are always correlated with ($\tilde{Q}_{2L} < 0$, $\tilde{Q}_{4L} > 0$) and ($\tilde{Q}_{2S} < 0$, $\tilde{Q}_{4S} > 0$), respectively. The opposite is also true for Q''_{4L} and Q''_{4S} . In addition, we note that the Λ_z^+ -scaled motion is found for $x^*/h = 25$, 50 and at least up to $x^*/h = 200$ of our data set; this suggests that the Λ_z^+ -scaled motion is prolonged in terms of streamwise evolution. Figures 4(g)–4(l) show the conditional fields of large- and small-scale components of the RSS further downstream ($x^*/h = 50$). Figures 4(g), 4(i), and 4(k) suggest that the organizations of the total RSS and coherent RSS, which are related to the fundamental mode (Λ_{z1}^+), are similar to that observed at $x^*/h = 25$, with greater intensities centered at slightly higher y/h . For the RSS counterparts related to subharmonic modes (Λ_{z2}^+), they are of lower RSS intensities compared to that observed at $x^*/h = 25$, as shown in Figs. 4(h), 4(j), and 4(l). A further discussion of this effect is provided in Sec. IV C.

B. Decomposition of mean skin friction generation due to RSS events

The relations between different decomposed quadrant events and mean skin friction generations ($C_{f,R}$), as mentioned in Sec. III, are assessed in Fig. 6 at $x^*/h = 25$. The premultiplied integrands

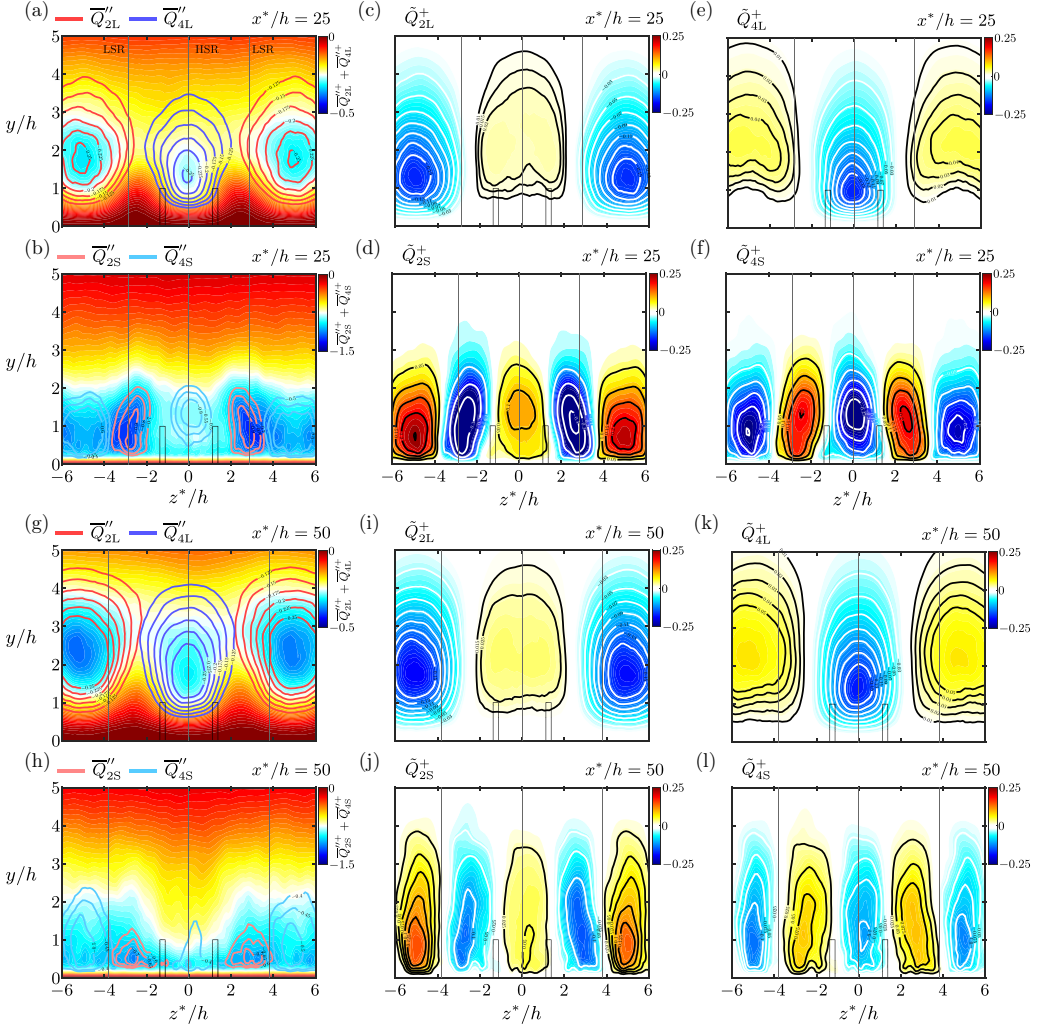


FIG. 4. (a), (g) Superposition of the conditional fields of the large-scale total RSS: $\bar{Q}''^+_{2L} + \bar{Q}''^+_{4L}$ at (a) $x^*/h = 25$ and (g) $x^*/h = 50$ (colour contour). Isolines represent the conditional large-scale ejection \bar{Q}''^+_{2L} (red) and sweep motions \bar{Q}''^+_{4L} (blue). (b), (h) Superposition of the small-scale counterparts: $\bar{Q}''^+_{2S} + \bar{Q}''^+_{4S}$ at (b) $x^*/h = 25$ and (h) $x^*/h = 50$ (colour contour). Isolines represent the conditional small-scale ejection \bar{Q}''^+_{2S} (light red) and sweep motions \bar{Q}''^+_{4S} (light blue). (c)–(f), (i)–(l) Contours of conditional fields of the coherent RSS associated with the (c), (e), (i), (k) large scales ($\lambda_z > \delta$) and (d), (f), (j), (l) small scales ($\lambda_z < \delta$) at (c)–(f) $x^*/h = 25$ and (i)–(l) $x^*/h = 50$. The vertical solid black lines mark the locations of high-speed region (HSR) and low-speed region (LSR) at $x^*/h = 25$ and 50, respectively.

show the majority of skin friction distributions in the wall-normal direction, where the area under each curve equals the contribution of each type of event to $C_{f,R}$, which is based on the decomposition presented in Sec. III. It can be seen that the major contributions to $C_{f,R}$ are generated by $f''_{R,2L}$, $f''_{R,4L}$, $f''_{R,2S}$, and $f''_{R,4S}$ (i.e., due to the Q''_2 and Q''_4 events), while the contributions from the Q''_1 and Q''_3 events are almost negligible. The peaks of $f''_{R,2L}$, $f''_{R,4L}$ are found at slightly higher wall-normal locations than the small-scale counterparts, as shown in Figs. 6(a) and 6(b). The integrands of the coherent components, which are generated due to secondary motions introduced by the MVG, particularly, $\tilde{f}_{R,2L}$, $\tilde{f}_{R,4L}$, $\tilde{f}_{R,2S}$, and $\tilde{f}_{R,4S}$, are of similar magnitudes and mainly generated

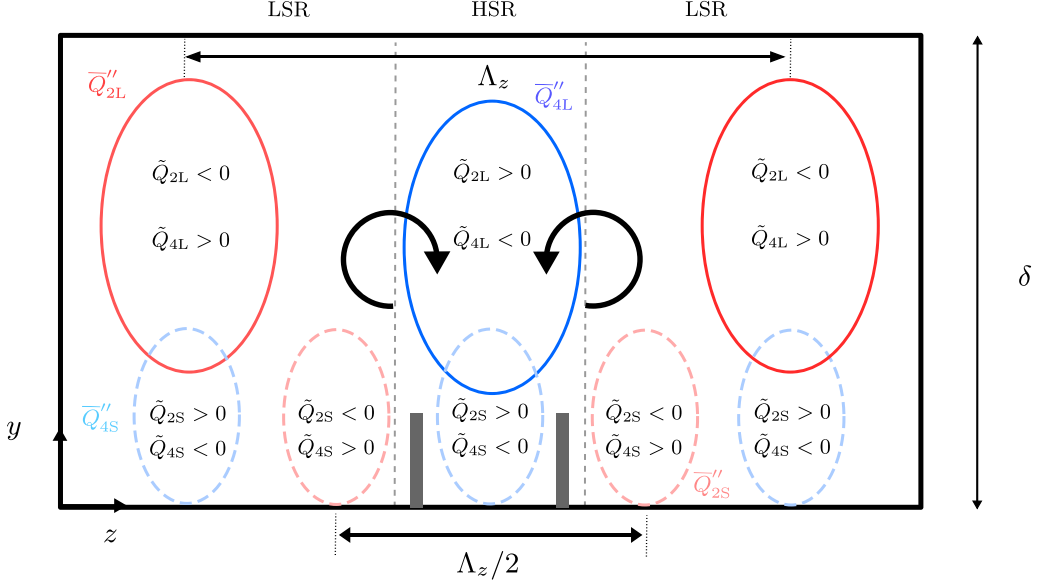


FIG. 5. Schematic illustration of the identified \bar{Q}_2'' and \bar{Q}_4'' and their observed correlations with \tilde{Q}_2 and \tilde{Q}_4 shown in Fig. 4. The Λ_z and $\Lambda_z/2$ reflect their spanwise characteristic length scales shown in Fig. 3.

in the region where $y/\delta < 0.3$ [shown in the inset in Figs. 6(a) and 6(b)]. The distributions of $\tilde{f}_{R,2L}$, $\tilde{f}_{R,4L}$, $\tilde{f}_{R,2S}$, and $\tilde{f}_{R,4S}$ suggest that the coherent components of the second and fourth quadrants contribute positively to $C_{f,R}$. The existence of the MVG leads to the generation of secondary motions and, therefore, the contribution to the skin friction drag. Figures 6(c) and 6(d) show the premultiplied integrands of the interaction components (LS and SL). It can be seen that, although these integrands cancel each other out in the mean sense (i.e., they do not have direct influence on $C_{f,R}$), they have individual non-negligible contributions to $C_{f,R}$, with the peaks located also at $y/\delta \simeq 0.3 - 0.4$ for the total and turbulent components, and peaks are located closer to the wall $y/\delta < 0.3$ for the coherent component. Figure 7 shows the integrand groups further downstream ($x^*/h = 50$). The small-scale integrands $f''_{R,nS}$, as shown in Fig. 7(b), collapse well with the $f''_{R,nS}$ because $\tilde{f}_{R,nS}$ are quickly diminished compared to the large-scale counterparts, which is shown in Fig. 7(a). This also indicates that the large-scale coherent RSS sustains longer than the small-scale coherent RSS.

Considering the $C_{f,R}$ decomposition developed in Sec. III, the mean skin friction coefficient due to RSS ($C_{f,R}$) is decomposed into contributions associated with different quadrant events. It has been shown that $C_{f,R}$ can be split based on Eq. (37), where $C''_{R,nL}$ are the mean skin friction components associated with large-scale quadrant events, and $C''_{R,nS}$ are the mean skin friction components associated with small-scale quadrant events. By the triple decomposition, we showed that $C''_{R,nL}$ and $C''_{R,nS}$ can be further decomposed into two groups, ($C'_{R,nL}$, $C'_{R,nS}$) and ($\tilde{C}'_{R,nL}$, $\tilde{C}'_{R,nS}$), representing the turbulent and coherent components of quadrant events, respectively. Their actual values are listed in Table I, in comparison with an unmanipulated (without MVGs) DNS TBL data set [31] (hereafter referred to as UBL) at two matched Reynolds numbers $Re_\tau \simeq 500$ and $Re_\tau \simeq 1000$. The values are directly computed by integrating the integrand groups over the wall. In this table, it is straightforward to sum across each row or sum across each column to obtain different contributions to $C_{f,R}$. For example, the sum of first four elements in the first column is equal to $\sum_{n=1}^4 C''_{R,nL}$ [see Eqs. (18) and (37)], representing the large-scale contribution to $C_{f,R}$ at the cutoff wave number $k_{z,c}$, while the the sum of first four elements in the second column is equal to the small-scale contribution to $C_{f,R}$. Meanwhile, the sum of the first four elements in the first

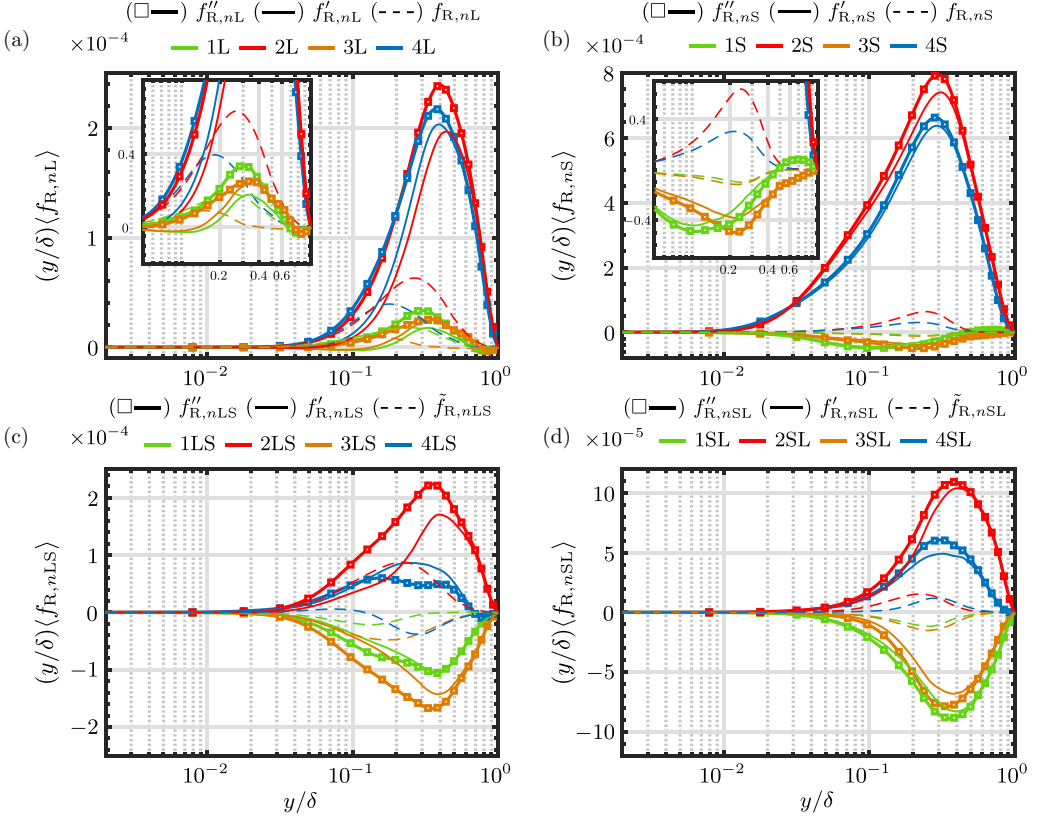


FIG. 6. Comparison of the premultiplied integrands contributing to $C_{f,R}$, between total RSS ($''$), turbulent RSS ($'$), and coherent RSS ($\tilde{\cdot}$) at $x^*/h = 25$ ($Re_\tau \simeq 470$) for (a) large scales (L), (b) small scales (S), (c), (d) large- and small-scale interactions (LS and SL).

row is equal to $C''_{R,1} = C''_{R,1L} + C''_{R,1S} + C''_{R,1LS} + C''_{R,1SL}$ [see Eqs. (33) and (41)], representing the Q'_1 contribution to $C_{f,R}$. The sum of the first four elements in the second row is equal to the Q'_2 contribution to $C_{f,R}$ and so forth. Additionally, it can be seen that the sums $\sum_{n=1}^4 C''_{R,nLS} = 0$ and $\sum_{n=1}^4 C''_{R,nSL} = 0$, showing no direct contributions to $C_{f,R}$. In a comparison between MVG2021 and UBL at $Re_\tau \simeq 500$, it is observed that there are significant differences in the coherent components: $\tilde{C}_{R,nL}$, $\tilde{C}_{R,nS}$, $\tilde{C}_{R,nLS}$, and $\tilde{C}_{R,nSL}$. These values are found to be very close to zero for the UBL case, while these values are larger in values in the MVG2021 case (highlighted in Table I at $Re_\tau \simeq 500$) because of the occurrence of the secondary motions induced by the MVG giving rise to the coherent components. The contributions of the coherent components decrease with increasing Re_τ , become similar to that in the UBL case at $Re_\tau \simeq 1000$. This is because the secondary motions are expected to decay in the downstream direction.

Another noticeable difference are the contributions in $C'_{R,nL}$ and $C'_{R,nS}$ between MVG2021 and UBL cases at $Re_\tau \simeq 500$. In particular, the contributions from the second and fourth quadrants small-scale turbulent RSS (i.e., $C'_{R,2S}$ and $C'_{R,4S}$, as highlighted in Table I) are increased by the MVG as compared to the UBL case. This may reflect how the large-scale vortice control responds differently to relatively low and high Reynolds numbers. As previously demonstrated by Canton *et al.* [32], who reported that, while the large-scale vortices induced a relaminarization effect to the flow for low Reynolds numbers ($Re_\tau = 104$ and 180) in the region where fluid is pushed toward the wall and can provide considerable drag reduction, the opposite effect was observed for a

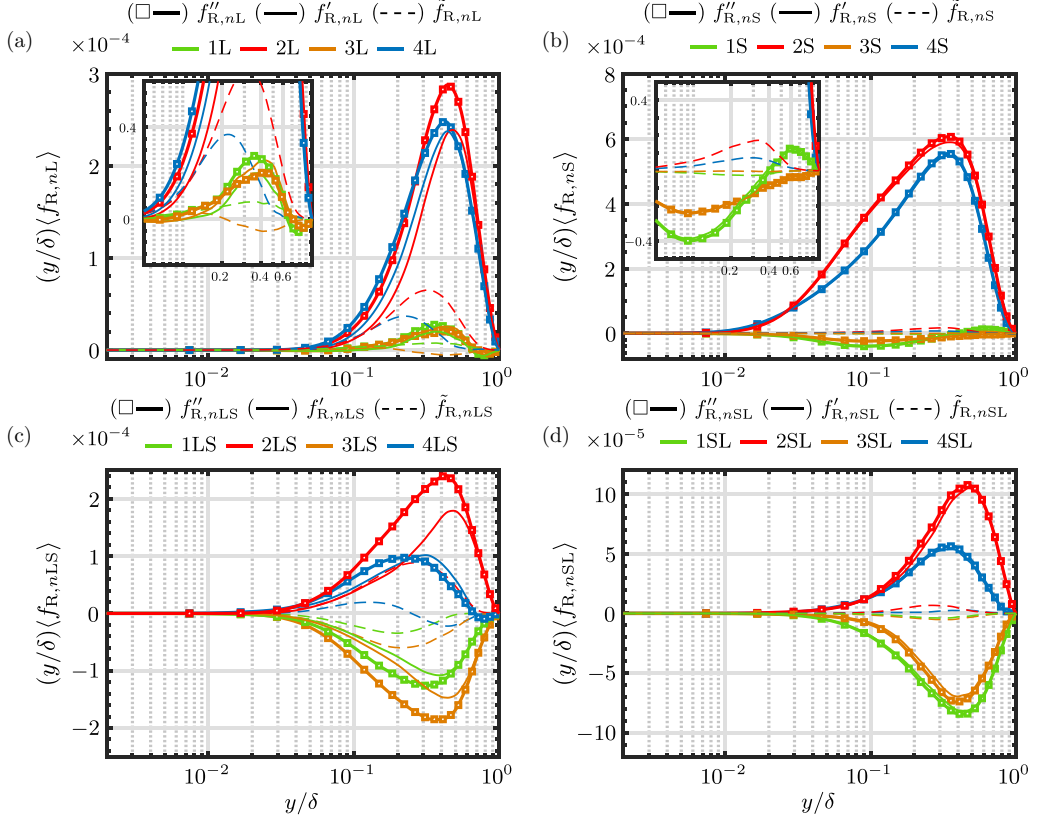


FIG. 7. Comparison of the pr-multiplied integrands contributing to $C_{f,R}$ between total RSS ($''$), turbulent RSS ($'$), and coherent RSS ($\tilde{\cdot}$) at $x^*/h = 50$ ($Re_\tau \simeq 500$), for (a) large scales (L), (b) small scales (S), and (c), (d) large- and small-scale interactions (LS and SL).

higher Reynolds number ($Re_\tau = 550$), i.e., the control method becomes ineffective to produce drag reduction and the method seems to increase the fluctuations in the wall-shear stress by promoting instabilities. Although there are fundamental differences between closed channel and TBL flows at higher Re_τ , the reported Re_τ , whereby the control method becomes ineffective, is similar to our case here ($Re_\tau \simeq 500$). Finally, the difference in the $C'_{R,nS}$ between MVG2021 and UBL cases becomes negligible at $Re_\tau \simeq 1000$ (also highlighted in Table I). This location is approximately at $x^*/h \simeq 500$, suggesting that only the increased large-scale turbulence persists a long downstream distance in terms of skin friction generation. In the next section (Sec. IV C), we will investigate this observation in further detail.

C. Inverse transfer of total RSS and Λ_+^+ -scaled mode interactions

From the results in Fig. 4, it seems that the intensity of the large-scale RSS events rises with downstream distance and only the small-scale events decay in the downstream direction. To further confirm this, we plot in Fig. 8(a) the root-mean-squared coherent RSS (\tilde{Q}_{2L}^+ , \tilde{Q}_{2S}^+ , \tilde{Q}_{4L}^+ , and \tilde{Q}_{4S}^+) at downstream locations $x^*/h = 25, 50$, and 200 , and Fig. 8(b) shows the evolution of the mean total RSS and the coherent RSS (i.e., \tilde{Q}_2 and \tilde{Q}_4), premultiplied by y . Figure 8(a) suggests a trend that the intensity of the large-scale coherent RSS grows with the downstream distance from $x^*/h = 25$ to $x^*/h = 50$, and after that it decreases further downstream, while the intensity of the small-scale coherent RSS shows a trend that it decreases monotonically from $x^*/h = 25$ to $x^*/h = 200$

TABLE I. ($\times 10^{-3}$) Skin friction generation by different components of the RSS events. n denotes the n th quadrant of (u'', v'') plane. Capital letter denotes the RSS events characterized as large scales (L), small scales (S), and large- and-small-scale interactions (LS and SL). (') denotes the total component, (") denotes the turbulent component, and (·) denotes the coherent component. Values in bold are discussed in the text. For the UBL case [31], the magnitudes estimated for $(C''_{R,nL}, C''_{R,nS}, C''_{R,nLS}, C''_{R,nSL})$ were very similar to those estimated for $(C'_{R,nL}, C'_{R,nS}, C'_{R,nLS}, C'_{R,nSL})$ and are not shown for brevity.

Case (Re $_{\tau}$)	n	$C''_{R,nL}$	$C''_{R,nS}$	$C''_{R,nLS}$	$C''_{R,nSL}$	$C'_{R,nL}$	$C'_{R,nS}$	$C'_{R,nLS}$	$C'_{R,nSL}$	$\check{C}_{R,nL}$	$\check{C}_{R,nS}$	$\check{C}_{R,nLS}$	$\check{C}_{R,nSL}$
MVG2021 (470)	1	0.042	-0.109	-0.214	-0.153	0.012	-0.093	-0.182	-0.138	0.031	-0.016	-0.033	-0.015
	2	0.346	1.657	0.415	0.176	0.247	1.571	0.255	0.155	0.100	0.087	0.160	0.020
	3	0.035	-0.103	-0.339	-0.120	0.023	-0.085	-0.243	-0.101	0.012	-0.019	-0.096	-0.020
	4	0.328	1.368	0.135	0.098	0.265	1.319	0.168	0.084	0.063	0.049	-0.033	0.013
MVG2021 (500)	1	0.030	-0.079	-0.251	-0.142	0.016	-0.074	-0.194	-0.137	0.013	-0.005	-0.057	-0.005
	2	0.375	1.457	0.429	0.159	0.282	1.431	0.269	0.150	0.093	0.027	0.160	0.009
	3	0.024	-0.061	-0.370	-0.107	0.025	-0.060	-0.255	-0.099	-0.002	-0.001	-0.115	-0.008
	4	0.353	1.206	0.193	0.090	0.301	1.193	0.182	0.086	0.052	0.013	0.011	0.004
UBL (520)	1					0.015	-0.074	-0.181	-0.121				
	2					0.262	1.226	0.248	0.137				
	3					0.020	-0.078	-0.222	-0.087				
	4					0.275	1.011	0.155	0.072				
MVG2021 (950)	1	0.019	-0.116	-0.177	-0.107	0.019	-0.112	-0.175	-0.106	0.000	-0.004	-0.001	-0.001
	2	0.202	1.247	0.216	0.117	0.201	1.226	0.215	0.116	0.001	0.021	0.001	0.001
	3	0.022	-0.124	-0.207	-0.081	0.022	-0.119	-0.205	-0.079	0.000	-0.005	-0.002	-0.002
	4	0.214	1.045	0.168	0.070	0.213	1.032	0.166	0.069	0.001	0.014	0.002	0.002
UBL (990)	1					0.017	-0.130	-0.144	-0.097				
	2					0.145	1.221	0.181	0.107				
	3					0.016	-0.139	-0.169	-0.070				
	4					0.157	1.036	0.132	0.060				

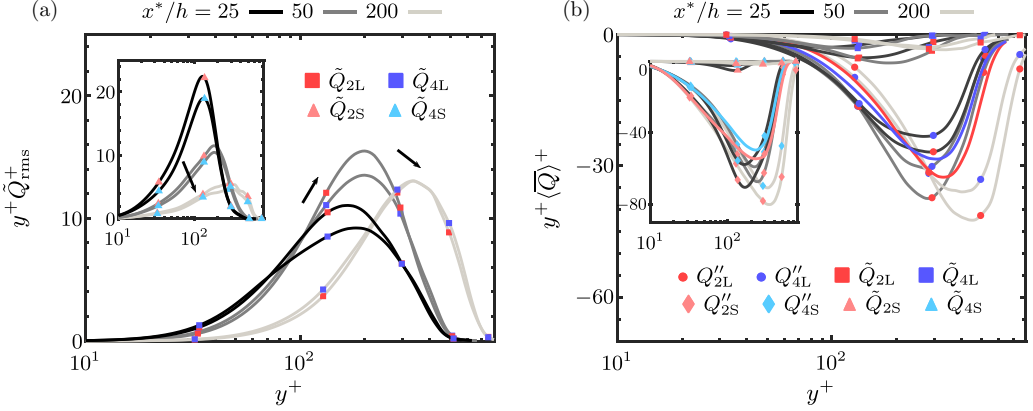


FIG. 8. (a) Streamwise evolution of the root-mean-squared coherent RSS for the second and fourth quadrants: $y^+ \tilde{Q}_{\text{rms}}^+$ of the large scales ($\lambda_z > \delta$) and in the inset plot the small scales ($\lambda_z < \delta$). Arrows in (a) indicate the trends with respect to x^*/h . (b) Premultiplied of the mean total RSS and coherent RSS for the second and fourth quadrants: $y^+ \langle \tilde{Q} \rangle^+$ of the large scales ($\lambda_z > \delta$) and in the inset plot the small scales ($\lambda_z < \delta$). In (b), solid lines colored according to the same color code represent the mean total RSS in the UBL case at $\text{Re}_\tau \simeq 500$.

[inset in Fig. 8(a)]. Despite that it is the limitation of our data set that makes it difficult to draw a clear conclusion about the trend of these intensities between $x^*/h = 25 - 50$, it has been demonstrated in Fransson and Talamelli [1] that the fundamental mode (i.e., Λ_z^+) shows a monotonic increasing energy level until it reaches $x^*/h = 100$, based on the streamwise velocity power spectral density, while the energy level of the first subharmonic mode ($\Lambda_z^+/2$) grows until it reaches $x^*/h = 40$, followed by an exponential decay further downstream. The monotonic decrease of the small-scale coherent RSS with the amplification of the intensity of the large-scale coherent RSS may help explain how organized high- and low-speed streaks can be sustained up to $x^*/h = 200$ downstream of the MVG when subjected to turbulence. A possible explanation for this may be attributed to the streaks interaction between neighboring MVG pairs through its subharmonic modes of motion. The following analysis aims to show that an inverse energy transfer occurs from the subharmonic modes (Λ_{z2}^+) to the fundamental mode (Λ_{z1}^+).

Finally, we provide partial evidence that supports the observation. We adopt the scale-by-scale transport of RSS budget equation, following the approach proposed by Kawata and Alfredsson [33]. The interscale Reynolds stress transports between small and large scales, taking the forms of

$$\text{Tr}_{ij} = \left\langle u''_{j,L} u''_{k,L} \frac{\partial u''_{i,S}}{\partial x_k} \right\rangle + \left\langle u''_{i,L} u''_{k,L} \frac{\partial u''_{j,S}}{\partial x_k} \right\rangle - \left\langle u''_{j,S} u''_{k,S} \frac{\partial u''_{i,L}}{\partial x_k} \right\rangle - \left\langle u''_{i,S} u''_{k,S} \frac{\partial u''_{j,L}}{\partial x_k} \right\rangle \quad (42)$$

and

$$\text{tr}_{ij} = - \frac{\partial \text{Tr}_{ij}}{\partial k_z}, \quad (43)$$

where the Reynolds stress fluxes Tr_{ij} represent a local transfer of $\langle u''_i u''_j \rangle$ between large and small-scale component at the cutoff wave number. The tr_{ij} , therefore, represent the net gain and loss of energy at each spanwise length scale through the Reynolds stress fluxes [33]. Kawata and Alfredsson [33] used this approach, and by using the Fourier mode decomposition on the Reynolds stress transport equations for plane Couette flow, they reported the small-scale dependence of RSS for large-scale structures. Figure 9 shows that there is an inverse energy transfer from the subharmonic modes Λ_{z2}^+ (i.e., $\Lambda_z^+/2$ and $\Lambda_z^+/3$) to the larger scales $\lambda_z^+ > \Lambda_z^+/2$. Two notable negative peaks representing inverse energy transfer are found at the first two subharmonic modes ($\Lambda_z^+/2$ and $\Lambda_z^+/3$) at $x^*/h = 25$, $y^+ \simeq 100$ [marked with \times in Figs. 9(a) and 9(b)], accompanied by an increased

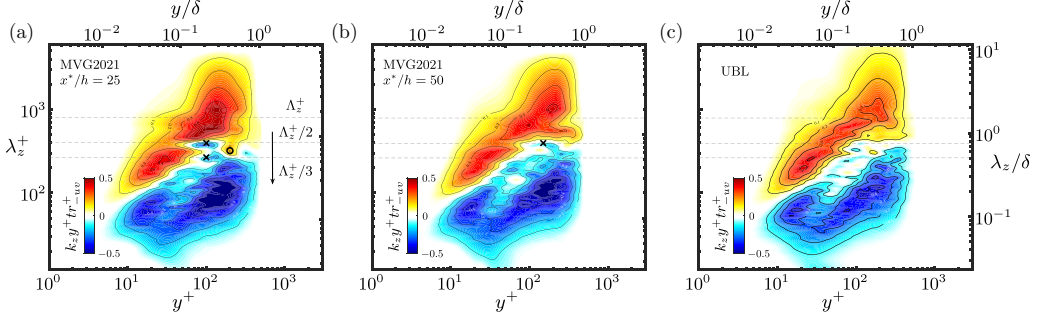


FIG. 9. The interscale transport of RSS, $k_z y^+ \text{tr}_{-uv}^+$ ($\text{tr}_{-uv}^+ = \text{tr}_{-uv} v/u_\tau^4$): (a) MVG2021 case at $x^*/h = 25$, (b) MVG2021 case at $x^*/h = 50$, and (c) UBL case (unmanipulated DNS TBL) at $\text{Re}_\tau \simeq 500$.

local gain of energy (higher tr_{-uv}) at the larger scales $\lambda_z^+ > \Lambda_z^+/2$, including the fundamental mode ($\Lambda_{z1}^+ = \Lambda_z^+$). The local energy gain at Λ_{z1}^+ is also shown to be enhanced at the near-wall region $y^+ < 100$ while, in the UBL case, such local energy gain at the wavelength $\lambda_z^+ \simeq \Lambda_z^+$ is less prominent and the inverse energy transfers at the subharmonic modes ($\Lambda_z^+/2$ and $\Lambda_z^+/3$) are clearly absent. In addition, at the outer region ($y^+ \simeq 200$), there is a region of relatively strong local energy gain at between the $\Lambda_z^+/2$ and $\Lambda_z^+/3$ (marked with a symbol \circ) that is absent in the UBL case. Further downstream ($x^*/h = 50$), the previously observed positive and negative peak values are decreased, however, a slightly negative peak persists at the first harmonic $\Lambda_z^+/2$. The result of Fig. 9(b) demonstrates that there is an increased local energy gain at wavelength $\lambda_z^+ \simeq \Lambda_z^+$ below $y^+ \simeq 250$ ($\sim 3h$) compared to the UBL case. Finally, the interscale transport for the MVG2021 case collapses well to that of the UBL case further downstream at approximately $x^*/h \simeq 1000$ (not shown). Overall, the inverse interscale transfer of RSS from small scales to large scales reveals a nontrivial scale interaction between Λ_{z1}^+ and Λ_{z2}^+ (more specifically, i.e., between Λ_z^+ , $\Lambda_z^+/2$, and $\Lambda_z^+/3$) that partially supports that the preservation of the Λ_z^+ -scaled motion is supported by its subharmonic modes of motions, which scale with $\Lambda_z^+/2$ and $\Lambda_z^+/3$. Results are also consistent with the trend of the coherent RSS intensities as presented in Fig. 8.

V. CONCLUSIONS

In this paper, we have investigated the influence of MVGs on the RSS in a moderate Reynolds number zero-pressure gradient TBL, using a data set obtained from a well-resolved large-eddy simulation [12]. We considered an approach based on the quadrant classification of the RSS events. The triple velocity decomposition and spanwise Fourier mode decomposition are then used in the quadrant classification to describe the flow modification by the MVGs in terms of different types of large- and small-scale RSS events at a given cutoff wavelength.

In our approach, we have shown sections of large- and small-scale conditional Q_2'' and Q_4'' quadrant event structures associated with LSRs and HSRs. The averaged properties of these quadrant events, such as mean skin friction generations $C_{f,R}$ under the influence of MVGs, are estimated through the FIK identity proposed by Fukagata *et al.* [16]. We have also shown how coherent RSS component arises due to the secondary motions induced by the MVG and we estimated their additional contributions to the mean skin friction coefficient in comparison with a unmanipulated turbulent boundary layer flow. In addition, we showed that the spanwise RSS modification is reflected on the energetic modes of the spanwise wave-number cospectra of $-u''v''$, $-u'v'$, and $-\tilde{u}\tilde{v}$, and the modification can be expressed by the superposition of the fundamental and subharmonic modes that scaled with the spanwise separation distance (Λ_z^+). A further analysis, based on the interscale transport of the RSS, proposed by Kawata and Alfredsson [33], showed that an inverse energy transfer from the subharmonics modes to the fundamental mode, suggesting that

the Λ_z^+ -scaled motion is partly sustained by its subharmonic modes of motions. The results provided insights into how large-scale motion of Λ_z^+ -scaled, which is introduced by the MVGs, is capable of persisting at distance of the order of $O(100h)$. Finally, the approach used in the present paper is generally applicable to other types of flows such as rough-wall bounded flows with spatial evolving heterogeneous surfaces.

ACKNOWLEDGMENTS

This research was undertaken with the assistance of resources provided at the NCI NF through the Computational Merit Allocation Scheme, supported by the Australian Government and the Pawsey Supercomputing Centre. Funds provided by the Australian Research Council are gratefully acknowledged.

-
- [1] J. H. M. Fransson and A. Talamelli, On the generation of steady streamwise streaks in flat-plate boundary layers, *J. Fluid Mech.* **698**, 211 (2012).
 - [2] S. Shahinfar, S. S. Sattarzadeh, J. H. M. Fransson, and A. Talamelli, Revival of Classical Vortex Generators Now for Transition Delay, *Phys. Rev. Lett.* **109**, 074501 (2012).
 - [3] J. H. M. Fransson, A. Talamelli, L. Brandt, and C. Cossu, Delaying Transition to Turbulence by a Passive Mechanism, *Phys. Rev. Lett.* **96**, 064501 (2006).
 - [4] S. Shahinfar, S. S. Sattarzadeh, and J. H. M. Fransson, Passive boundary layer control of oblique disturbances by finite-amplitude streaks, *J. Fluid Mech.* **749**, 1 (2014).
 - [5] S. S. Sattarzadeh, J. H. M. Fransson, A. Talamelli, and B. E. G. Fallenius, Consecutive turbulence transition delay with reinforced passive control, *Phys. Rev. E* **89**, 061001(R) (2014).
 - [6] O. Lögdberg, Vortex generators and turbulent boundary layer separation control, Licentiate thesis, Department of Mechanics, KTH, Stockholm, 2006.
 - [7] O. Lögdberg, J. H. M. Fransson, and P. H. Alfredsson, Streamwise evolution of longitudinal vortices in a turbulent boundary layer, *J. Fluid Mech.* **623**, 27 (2009).
 - [8] O. Coceal and S. E. Belcher, A canopy model of mean winds through urban areas, *Q.J.R. Meteorol. Soc.* **130**, 1349 (2004).
 - [9] H. M. Nepf, Flow and transport in regions with aquatic vegetation, *Annu. Rev. Fluid Mech.* **44**, 123 (2012).
 - [10] O. Coceal, T. G. Thomas, I. P. Castro, and S. E. Belcher, Mean flow and turbulence statistics over groups of urban-like cubical obstacles, *Boundary-Layer Met.* **121**, 491 (2006).
 - [11] S. Shahinfar, J. H. M. Fransson, S. S. Sattarzadeh, and A. Talamelli, Scaling of streamwise boundary layer streaks and their ability to reduce skin-friction drag, *J. Fluid Mech.* **733**, 1 (2013).
 - [12] C. I. Chan and R. C. Chin, Investigation of the influence of miniature vortex generators on the large-scale motions of a turbulent boundary layer, *J. Fluid Mech.* **932**, A29 (2022).
 - [13] B. Ganapathisubramani, N. Hutchins, W. T. Hambleton, E. K. Longmire, and I. Marusic, Investigation of large-scale coherence in a turbulent boundary layer using two-point correlations, *J. Fluid Mech.* **524**, 57 (2005).
 - [14] M. Guala, S. E. Hommema, and R. J. Adrian, Large-scale and very-large-scale motions in turbulent pipe flow, *J. Fluid Mech.* **554**, 521 (2006).
 - [15] B. Balakumar and R. Adrian, Large- and very-large-scale motions in channel and boundary-layer flows, *Phil. Trans. R. Soc. Lond. A* **365**, 665 (2007).
 - [16] K. Fukagata, K. Iwamoto, and N. Kasagi, Contribution of Reynolds stress distribution to the skin friction in wall-bounded flows, *Phys. Fluids* **14**, L73 (2002).
 - [17] M. de Giovanetti, Y. Hwang, and H. Choi, Skin-friction generation by attached eddies in turbulent channel flow, *J. Fluid Mech.* **808**, 511 (2016).
 - [18] J. M. Wallace, Quadrant analysis in turbulence research: History and evolution, *Annu. Rev. Fluid Mech.* **48**, 131 (2016).

- [19] E. R. Corino and R. S. Brodkey, A visual investigation of the wall region in turbulent flow, *J. Fluid Mech.* **37**, 1 (1969).
- [20] J. Kim, P. Moin, and R. Moser, Turbulence statistics in fully developed channel flow at low Reynolds number, *J. Fluid Mech.* **177**, 133 (1987).
- [21] R. D. Moser, J. Kim, and N. N. Mansour, Direct numerical simulation of turbulent channel flow up to $Re_\tau = 590$, *Phys. Fluids* **11**, 943 (1999).
- [22] S. S. Lu and W. W. Willmarth, Measurements of the structure of the Reynolds stress in a turbulent boundary layer, *J. Fluid Mech.* **60**, 481 (1973).
- [23] S. S. Sattarzadeh and J. H. M. Fransson, On the scaling of streamwise streaks and their efficiency to attenuate Tollmien–Schlichting waves, *Exp. Fluids* **56**, 58 (2015).
- [24] D. Goldstein, R. Handler, and L. Sirovich, Modeling a no-slip flow boundary with an external force field, *J. Comput. Phys.* **105**, 354 (1993).
- [25] M. Chevalier, A. Lundbladh, and D. S. Henningson, SIMSON—A pseudo-spectral solver for incompressible boundary layer flow, Technical Report No. TRITA-MEK 2007:07 (KTH Mechanics, Stockholm, Sweden, 2007).
- [26] P. Schlatter, S. Stolz, and L. Kleiser, LES of transitional flows using the approximate deconvolution model, *Int. J. Heat Fluid Flow* **25**, 549 (2004).
- [27] S. Stolz, N. A. Adams, and L. Kleiser, An approximate deconvolution model for large-eddy simulation with application to incompressible wall-bounded flows, *Phys. Fluids* **13**, 997 (2001).
- [28] G. Eitel-Amor, R. Örlü, and P. Schlatter, Simulation and validation of a spatially evolving turbulent boundary layer up to $Re_\theta = 8300$, *Int. J. Heat Fluid Flow* **47**, 57 (2014).
- [29] P. Schlatter, Q. Li, G. Brethouwer, A. V. Johansson, and D. S. Henningson, Simulations of spatially evolving turbulent boundary layers up to $Re_\theta = 4300$, *Int. J. Heat Fluid Flow* **31**, 251 (2010).
- [30] P. Schlatter and R. Örlü, Turbulent boundary layers at moderate Reynolds numbers: Inflow length and tripping effects, *J. Fluid Mech.* **710**, 5 (2012).
- [31] C. I. Chan, P. Schlatter, and R. C. Chin, Interscale transport mechanisms in turbulent boundary layers, *J. Fluid Mech.* **921**, A13 (2021).
- [32] J. Canton, R. Örlü, C. Chin, and P. Schlatter, Reynolds number dependence of large-scale friction control in turbulent channel flow, *Phys. Rev. Fluids* **1**, 081501(R) (2016).
- [33] T. Kawata and P. H. Alfredsson, Inverse Interscale Transport of the Reynolds Shear Stress in Plane Couette Turbulence, *Phys. Rev. Lett.* **120**, 244501 (2018).